PAPER

Zirconium-based MOFs as pH-responsive drug delivery systems: encapsulation and release profiles of ciprofloxacin

Muhammad Ishfaq,[a] Dilawar Lateef,[a] Zohaib Ashraf,[a] Muhammad Sajjad,[a] Muhammad Owais,[a] Waseem Shoukat,[a] Muhammad Mohsin,[a] Muhammad Ibrahim,[b] Francis Verpoort [iD][cd] and Adeel Hussain Chughtai [iD] *[a]

As antimicrobial resistance (AMR) continues to rise, the need for improved antibiotic delivery systems is urgent to prevent overexposure from systemic administration. To address this clinical trial, metal–organic frameworks have developed as promising contender for regulated drug release. In this study, ciprofloxacin (CIP) was encapsulated into two zirconium-based MOFs (ZrMOF-1 and Zr-MOF-2), synthesized *via* a previously reported solvothermal method. Comprehensive characterization was performed using FTIR, PXRD, SEM, and BET analysis confirming their crystallinity and porosity. The MOFs structure integrity was maintained even after drug loading, ensuring stability. Ciprofloxacin release profiles were monitored *via* UV-Vis spectroscopy, revealing that MOF-2 exhibited more controlled and sustained release over seven days in a basic medium (pH 9.2). A pH-responsive release behavior was observed, with accelerated drug release in basic conditions, suggesting a tunable release mechanism. These findings confirm that Zr-MOF@CIP is a potential biocompatible material for drug delivery systems, warranting further *in vivo* studies for applications in medical science and pharmaceutics.

1 Introduction

Drug carriers play a crucial role in modern medicine by addressing challenges such as drug instability, poor solubility, and ineffective targeting. The need for effective drug delivery systems has been evident throughout history, from ancient civilizations to the present day. Early treatments using natural substances from plants addressed basic ailments,[1] but the complexity of diseases like bacterial infections required more advanced solutions. The discovery of antibiotics like penicillin in the early 20th century revolutionized medicine, offering effective treatments against bacterial diseases.[2] However, the emergence of drug-resistant bacteria highlighted the need for innovative approaches. Ciprofloxacin, a potent fluoroquinolone antibiotic, has emerged as a cornerstone in the medical treatments against many bacterial infections.[3] Ciprofloxacin exhibits wide ranging effectiveness against Gram negative and positive bacteria by targeting prokaryotic DNA gyrase and Topo IV, crucial enzymes involved in DNA replication phase and its repairing.[4] Its effectiveness is crucial in treating many bacterial infections, but optimizing its delivery remains a challenge.

Drug carriers include a diverse array of antibacterial materials such as metal-based nanomaterials,[5–7] (*e.g.*, copper, silver, zinc), organic compounds,[8] semiconductor photocatalyst,[9,10] liposomes, polymeric micelles,[11] microspheres[12] and nano-diamonds.[13,14] Over the years, various materials have been explored for their antibacterial properties, yet many remain far from clinical application due to inherent limitations metal-based nano-materials and organic compounds combat bacteria by emitting toxic metal clusters or antibacterial substances, but their effectiveness is often limited by the rapid release of active substances, which may also pose risks to living organisms. Semiconductor photocatalytic materials offer another approach, utilizing light-induced charge carriers to enhance enzymes like activity for bacterial elimination. However, their effectiveness is constrained by limited light absorption and low catalytic efficiency, reducing their antibacterial potential. Natural biological antibacterial materials, derived from plants or animals, provide a safer and more biocompatible alternative, requiring minimal modification for therapeutic use. Nevertheless, the scarcity of sources, high extraction costs, and intricate processing methods restrict their widespread application in clinical settings. Despite their promise, these materials face significant challenges that must be addressed to transition effectively into clinical practice.

[a] Institute of Chemical Sciences, Bahauddin Zakariya University, Multan 60800, Pakistan. E-mail: adeelhussain@bzu.edu.pk; Tel: +92-3339702072

[b] Department of Biochemistry, Bahauddin Zakariya University, Multan 60800, Pakistan

[c] Joint Institute of Chemical Research (FFMiEN), Peoples Friendship University of Russia (RUDN University), Moscow 117198, Russia

[d] Laboratory of Organometallics, Catalysis and Ordered Materials, State Key Laboratory of Advanced Technology for Materials Synthesis and Processing, Center for Chemical and Material Engineering, Wuhan University of Technology, Wuhan 430070, China. E-mail: francis@whut.edu.cn; Tel: +86-18701743583

Liposomes are useful for delivering a variety of drugs of differing lipophilicity. Nevertheless, they show limited control over drug release, with drugs potentially leaking due to high membrane permeability and slow, inefficient diffusion processes. Polymeric micelles serve as drug carriers formed through the self-assembly of amphiphilic molecules containing an amphiphilic block co-polymer. They assemble at a defined micelle concentration, which can be reduced by the block copolymer. However, their absence of an aqueous core limits their ability to accommodate a broad range of drugs compared to liposomes. In contrast, microspheres are hollow, micron-scale carriers that originate from the self-organization of polymeric materials, used to encapsulate active drugs. Drug release is typically achieved through diffusion or degradation of the microsphere shell. Microspheres face limitations including difficulties in achieving precise and uniform drug release rates, potential for burst release, and challenges with scaling up production. Variability in microsphere size and complex fabrication methods can also hinder their effectiveness. Nano-diamonds (NDs) are carbon nanoparticles ranging from 4 to 100 nm in diameter, fabricated through elevated pressure and temperature (HP-HT NDs) or by shock-wave compression method (detonation nanodiamonds, DNDs). Additionally, surface modifications, including oxidation and size reduction, can significantly alter their adsorption properties. However, potential toxicity and the complexity of surface modifications pose challenges for effective drug delivery.

Biomimetic strategies, such as protein nanocages and cell membrane camouflage, represent innovative pathways in anti-bacterial drug development. Ferritin, a protein with reverse self-organization properties, has been exploited to form artificial nanocages with internal chambers for drug encapsulation. These positively charged nanostructures effectively target bacteria but face limitations in encapsulating larger drug molecules due to their nanoscale dimensions.[15] Additionally, current protein encapsulation techniques lack the precision required for accurate loading of functional substances. On the other hand, cell membrane camouflage leverages the complex biological components of natural membranes to help drugs evade immune detection, prolong circulation in the bloodstream, and enhance delivery to infection sites. Despite these advantages, the technique still suffers from low screening efficiency for natural compounds and inadequate stability to function in the intricate physiological environment. Addressing these obstacles is crucial to unlock full potentials of these biomimetic technologies in clinical applications.

In recent years, the focus on designing innovative drug delivery systems has highlighted the potential of MOFs (Metal–Organic Frameworks) and their derivatives in the antimicrobial field due to their tunable structures and adjustable sizes. MOFs are highly porous materials consist of metal ions or clusters, which serve as coordination nodes, and poly-dentate ligands, which act as linker connecting these nodes through coordination bonds. These bonds form networks that exhibit zero-dimensional,[16] one-dimension,[17] two-dimensions,[18,19] or three-dimensions architectures.[20] The primary structural features of MOFs, directly linked to their applications, include high porosity with pore volumes reaching up to 90% of the crystalline structure, large specific surface areas exceeding several thousand square meters per gram,[21] O, and thermal stability ranging from 250–500 °C (ref. 22) attributed to strong bonds including carbon–carbon single bond, carbon–hydrogen single bonding, carbon–oxygen single bonding, and metal–oxygen single bonding. These unique properties position MOFs as promising candidates for advanced antimicrobial and drug delivery applications.

High surface area, high porosity, tunability, structural versatility, encapsulation capability, controlled release, and biocompatibility enable the metal–organic frameworks (MOFs) to be used in variety of applications. They are employed in gas storage and separation,[23–25] efficiently capturing and selectively separating gases like hydrogen, methane, and carbon dioxide,[26,27] molecular identification,[28] separation,[29] treatments and diagnosis in biomedical science,[30,31] renewable energy,[32,33] thin film systems,[34] adsorption,[35] magnetic attraction,[36–38] bio-gass green energy,[39] catalysis,[40–43] luminescence,[44] proton conduction,[45] sensing,[46] delivery of medications,[47,48] carbon capture,[49] solar power cells,[50] water splitting,[51] ORR,[52] HER,[53] OER[54–58] and a diverse array of remarkable properties is imparted to MOFs structures through the presence of multifunctional ligand-based bridging units.

Metal–organic frameworks are beneficial in different types of chemical processes[59] as they have tunable pore sizes and large external surfaces. In drug delivery systems they present controlled release and targeted therapy owing to their ability to encapsulate therapeutic agents. They are also applied in environmental applications where pollutants have to be removed and sensing and detection of chemical or biological agents.[60–62] It is used in imaging modalities;[63] it is involved in water purification by removing particulate matter.[64–66] These diverse applications show the importance of MOFs in the various fields of science and industries.

In recent years, varieties of MOFs have been utilized as different drugs carrier for controlled drug release, offering several advantages as newly developed materials. The nanoscale size of MOFs can be precisely controlled, enabling efficient drug uptake and penetration through cellular membrane. The potential toxicity of MOFs can be sensitively avoided by selecting non-toxic metals and ligands. Additionally, high drug loading capacities and a high density of polar sites of MOFs enable sustained drug release over extended periods. Furthermore, MOF-based drug carriers can exhibit pH responsiveness due to the pH-dependent stability of certain MOFs, making them effective for targeted drug delivery in specific biological environments.

The cambridge structural database (CSD) has roughly synthesized 99 075 MOF and MOF-type compounds. Ionic MOFs have recently provided an innovative way for drug delivery. An et al., utilized bio-MOF as a carrier for procainamide, achieving a uptake capacity of 0.22 g g^{-1}.[67] In 1995, the Yaghi group studied guest molecule binding in a microporous MOF composed of cobalt cations and 1,3,5-benzene tricarboxylate (BTC).[68] In 1999, they reported MOF-5, constructed with 1,4-benzenedicarboxylate (BDC) ligands and Zn_4O clusters, offering

a Langmuir surface area of 2900 m^2 g^{-1}.[69] Sun *et al.* described the anionic MOF ZnTATAT, derived from DMF decomposition in its channels, which loaded the neutral anticancer drug 5FU with a capacity of 0.5 g g^{-1}.[70] Hu *et al.* developed MOF-74Fe(III) through post-oxidation, enabling it to encapsulate ibuprofen anions with a capacity of 0.19 g g^{-1}. However, the particle size of MOF-74Fe(III), approximately 2 micrometers, makes it unsuitable for intravenous administration, limiting its application to oral drug delivery.[71] Jiang *et al.* synthesized anionic MOF ZJU-64-NSN for selective drug adsorption, achieving a loading capacity of 21% for procainamide (PA) due to strong electrostatic attraction, and demonstrated controlled release influenced by pH and sodium ions.[72] Dong and his team synthesized folic acid-functionalized Zr-based MOFs, achieving drug loading efficiencies of 38.42% and 30.26% for MOF-808 and NH$_2$-UiO-66, respectively, with promising dose-dependent responses in cancer therapy.[73] In our previous work, we synthesized two types of Cu-MOFs : MOF with single-linker (BPDC) entitled as Cu-MOF(s) and MOF with mixed linkers (BPDC and BPY) entitled as Cu-MOF(m). Cu-MOF(m) exhibited a larger pore volume indicated by N$_2$ sorption isotherms and higher surface area (1498.31 m^2 g^{-1}) compared to Cu-MOF(s) (surface area 534.3 m^2 g^{-1}), leading to better drug loading efficiency. Ibuprofen and montelukast sodium were encapsulated in these MOFs, with CuMOF(m)@Ibu (2 : 1) exhibiting the extreme drug uptake. The sustained releasing of Ibu demonstrated an initial burst release followed by a slower release, particularly from Cu-MOF(m), which had stronger interactions between Cu(II) sites and the drug. The release of meS was less efficient due to its larger size. FTIR analysis confirmed strong drug-MOF interactions. Cu-MOF(m) outperformed Cu-MOF(s) in both drug loading and release, highlighting the importance of MOF structure in drug delivery.[48]

Zr-MOFs, notably UiO-66 discovered by Cavka *et al.*, in 2008 (ref. 74) have achieved noteworthy attention because of their unparalleled stability, especially in hydrothermal and acidic environments, ascribed to strong coordination linkage between Zr(IV), and carboxylate ligands. Their high surface area and porosity allow for significant drug loading, enhancing the efficiency of drug delivery. Additionally, Zr is naturally abundant and exhibits low toxicity, making these frameworks suitable for biomedicine.[75,76] Surface chemistry modifications, such as introducing functional groups like –NH$_2$ and –NO$_2$, impact drug loading capacity and release behavior, with –NH$_2$ functionalized UiO-66 exhibiting maximal loading and slower release rates due to strong hydrogen bond abilities.[77] Another variant, Zr-BPDC, featuring an endogenous 4,4′-biphenyldicarboxylic acid as organic linker, shows enhanced porosity, biocompatibility and efficient drug transport capabilities making it a promising drug delivery system (DDS).

Because of these advantages of Zr-MOF, a comprehensive study on the encapsulation and release characteristics of ciprofloxacin using a Zr based metal organic frameworks (Zr-MOFs) as a nano-carrier is conducted. The release of ciprofloxacin from metal–organic frameworks (MOFs) has got significant interest in the context of drug delivery due to tunable properties of MOFs that can enhance drug loading and control

release rates. In this work, we investigate two zirconium-based MOFs which differ in their organic linker composition and consequently their physical characteristics, such as larger surface area and pore volume ratio. These differences significantly influence their drug loading capacity and release profiles for ciprofloxacin hydrochloride, a broad-spectrum antibiotic with acidic characteristics. The focus is on exploring the encapsulation efficiency and loading capacity of ciprofloxacin in MOFs at various MOF : drug ratios (1 : 1, 1 : 2, and 1 : 3). Additionally, the release of ciprofloxacin at three distinct pH environments (9.2, 7.4, and 3.0) are examined. The investigation includes detailed analyses of the interactions between ciprofloxacin and the MOFs, the stability of the drug-MOF complex, and the influence of pH on the drug release profile. By systematically assessing these parameters, the study aims to provide a thorough understanding of capability of MOFs as advanced drug delivery systems, highlighting their capacity to enhance the solubility, stability, and controlled release of ciprofloxacin for various therapeutic uses.

2 Experimental

2.1 Materials and method

2-Aminobenzene-1,4-dicarboxylic acid, zirconium oxychloride octahydrate, 4,4′-biphenyl-dicarboxylic acid, ciprofloxacin hydrochloride, DMF (*N*,*N*′-dimethylformamide), sodium chloride, potassium chloride, monosodium phosphate (MPS), potassium dihydrogen phosphate, acetic acid, sodium acetate and ethanol were obtained from Merck and utilized without any more purification. Throughout the experiment, double deionized water was exclusively utilized. Fourier transform infrared (FTIR) spectra have measured using Agilent Technologies 41 630 spectrometer. The peaks in PXRD (Powder X-ray Diffraction) patterns have analyzed employing a D8 advanced Bruker–Powder–Diffractometer equipped with Cu Kα radiation. BET measurements' pore size and surface area have been carried out at 77 K using nitrogen (N$_2$) sorption isotherms using a Micromeritics ASAP 2020 apparatus. Before analysis, preparing Cu-MOF was subjected to prolonged degassing over night at a temperature of 150 °C. Scanning electron microscopy (SEM) analyses were conducted utilizing the JSM740 scanning electron microscope.

2.2 Synthesis of MOFs

The previously reported solvothermal method was used to synthesize the Zr-MOFs with slight modification.[78–80] In a representative method, 20 mL of DMF was blend with 1 mmol of NH$_2$-BDC (2-amino-1,4-benzenedicarboxylic acid) in a Teflon-lined cup and stirred for 10 minutes. One millimole of zirconium oxychloride octahydrate was added in above solution and followed by an additional 10 minutes of stirring, after which 20 mL of formic acid was added into the mixture. The obtained solution containing Teflon cup was put into an autoclave and subjected to heating at 120 °C for 72 hours. Subsequently end of reaction time, the Teflon was let to cool. Finally, resulting solid was separated by filtration, washed extensively with DMF solvent and

then dried at 100 °C to yield yellow slid as Zr MOF-1. The formation of Zr MOF-2 was alike to Zr-MOF-1 except that 4,4′-biphenyldicarboxylic acid (BPDC) was used instead of NH_2-BDC.

2.3 Activation of MOFs

To improve porosity, adsorption and drug-loading capacity, activation of Zr-MOFs is essential, particularly to remove the trapped high boiling point solvents like DMF, which can impair performance. Activation of both MOFs was achieved through a solvent exchange method. Zr-MOF-1 was immersed in 10 mL of ethanol in a glass ampoule and kept for 24 hours. The ethanol was then replaced with fresh ethanol, repeating the process three times. Subsequently, the ethanol was decanted, and trichloromethane was added to the vial. This solvent exchange with trichloromethane was also conducted every 24 hours for three cycles. The activated material was obtained by filtration and drying at room temperature. The same procedure was used to activate Zr-MOF-2.[81,82]

2.4 Encapsulation of ciprofloxacin

To incorporate ciprofloxacin onto the synthesized Zr-MOFs at Zr-MOF : drug ratios of 1 : 1, 1 : 2, and 1 : 3 (corresponding to 60 mg, 120 mg, and 180 mg of ciprofloxacin in separate glass vial respectively), ciprofloxacin was dissolved in double distilled water to make solutions of required concentrations. Then, 60 mg of the respective Zr-MOF was added in each glass vial. Each mixture was thoroughly stirred for 12 hours to ensure uniform distribution and facilitate adsorption of ciprofloxacin onto the Zr-MOF. The ciprofloxacin-loaded Zr-MOFs (zirconium-MOF-1@CIP and zirconium-MOF-2@CIP) were recovered by filtration and centrifugation. The loaded MOFs were washed with water and ethanol to remove unbounded drug particles. Finally, they were dried at 80 °C to produce a free-flowing powder. The percentage of loading (PL%) was calculated using the formula provided below.

$$PL\% = \frac{\text{weight of drug loaded MOF A} - \text{weight of MOF A}}{\text{weight of drug used}} \times 100$$

2.5 Release of drug from drug loaded MOF (Zr-MOF@CIP)

The Zr-MOF nanoparticles loaded with the drug were embedded in 10 mL of buffered solutions at different pH values of 3.0, 7.4 (PBS), and 9.2. At regular interludes, 1 mL of each solution was taken out using a 5 mL syringe fitted with a syringe filter, and an equal volumes of fresh buffer solutions was put to maintain consistency. The released drug concentration was measured via UV-Vis spectroscopy at 276 nm. The percentage release (PR%) was calculated by means of formula provided below.

$$PR\% = \frac{\text{amount of drug released in consecutive times (mg)}}{\text{initial drug mass in nanocarrier (mg)}} \times 100$$

2.6 Preparation of buffer solutions

To prepare a phosphate buffer solution (pH 7.4), 200 mg of KCl, 8 grams of NaCl, 1.044 grams of NaH_2PO_4, and 240 mg of KH_2PO_4 were dispersed in almost 800 mL of deionized water. The final volume was brought up to 1000 mL. The buffer solutions; basic buffer (pH 9.4) and acidic buffer (pH 3.0) were prepared following the Henderson–Hasselbalch equation.

$$pH = pK_a + \log\frac{[\text{sodium acetate}]}{\text{acetic acid}}$$

3 Results and discussion

3.1 Characterization of Zr-MOFs

The successful synthesis of Zr-MOFs was examined by PXRD as given in Fig. 1. The PXRD pattern shows peaks at around $2\theta = 7.4°$, 8.5°, 12°, 14.1°, 14.7°, 17°, 18.6°, 19.1°, 22.2°, 25.6°, 28.3°, 30.6°, 33°, 35.5°, 37.4°, 40.6°, and 43.27. The values of XRD peaks correspond to (1 1 1), (2 0 0), (2 2 0), (3 1 1), (2 2 2), (4 0 0) (3 3 1), (4 2 0), (5 1 1), (6 0 0), (5 3 3), (7 1 1), (7 3 1), (8 2 0), (7 5 1), (6 6 4), and (9 3 3) Miller planes examined in P-XRD pattern of our synthesized Z-MOF-1 and correspond to the construction of amino-functionalized UiO-66 consistent with the PXRD patterns of the NH_2-UiO-66 MOF and the simulated one (CCDC No. 889529) reported values in previous literature confirming that Zr-MOF-1 framework is iso-structural to prototype UiO-66 Zr-MOFs family.[74,83] The main characteristic diffraction peaks of samples ($2\theta = 7.4°$, 8.6° and 25.6°, labeled with *) showed good agreement with those reported in existing literature. The prominent peaks at lower angle ($2\theta = 7.31°$ and 8.51°), which correspond to the first and second diffractions peak, (1 1 1) and (2 0 0), correspond to the extended-octahedral and super-tetrahedral cavities. The presence of distinct sharp peaks in PXRD patterns of Zr-MOF-1 indicates a high degree of crystallinity and contains pure phases with no distinctive peaks associated with the impurities. In case of Zr-MOF-2, all diffraction peaks in P-XRD spectra at $2\theta = 5.7°$, 6.6°, 9.3°, 10.8, 11.4°, 19.6° and 30.4° are in good agreement with PXRD peak pattern of UiO-67, already reported in the literature, shown effective formation of Zr-MOF.[84,85] The values of XRD peaks correspond to (1 1 1), (2 0 0), (2 2 0), (3 1 1), (2 2 2) and (6 0 0) lattice planes. Sharp PXRD peaks validated the synthesized Zr-MOF high crystallinity and proving the high purity of the synthesized material.

FTIR spectra of both MOFs are presented in Fig. 2, 2-amino-BDC, 4,4′-biphenyldicarboxylic acid, ciprofloxacin (CIP) and ciprofloxacin loaded Zr-MOF (zirconium-MOF-1@CIP, zirconium-MOF-2@CIP). The bands at 1606 cm^{-1} and 1432 cm^{-1} correspond to asymmetrical and symmetrical stretches of carboxylates group, which interact with Zr^{4+}. The NH_2-BDC linker exhibits weak bands at 3387 cm^{-1} and 3498 cm^{-1}, ascribed to symmetric and asymmetric NH_2 vibrations. Additionally, characteristic stretching between the amine nitrogen and aryl carbon appears at 1400 cm^{-1} and 1225 cm^{-1}. The IR spectra also confirm the loading of ciprofloxacin (CIP) into
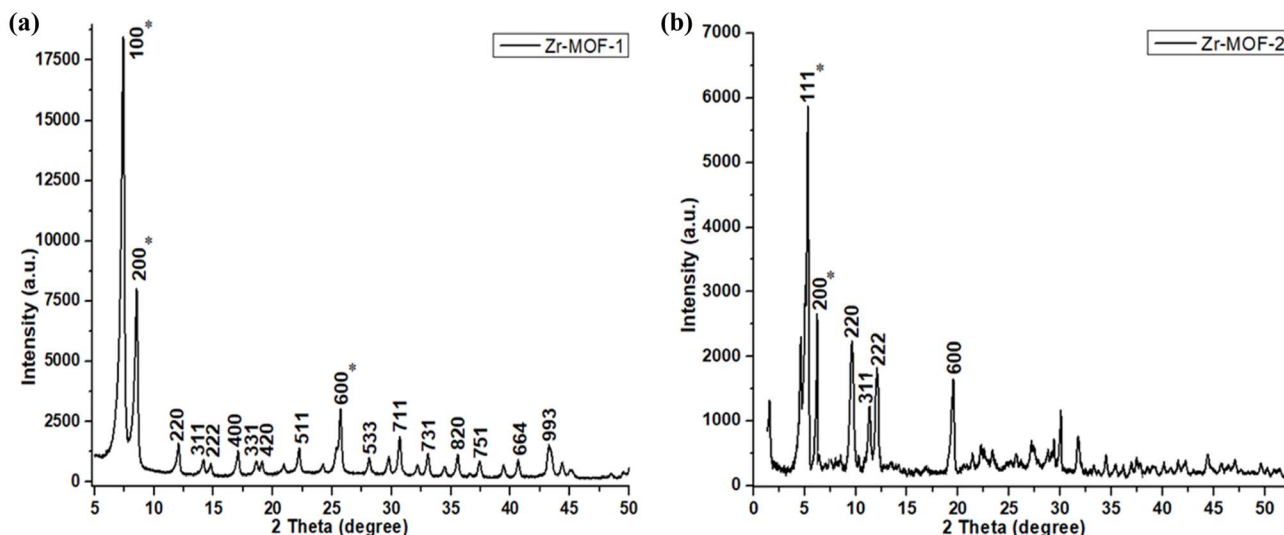
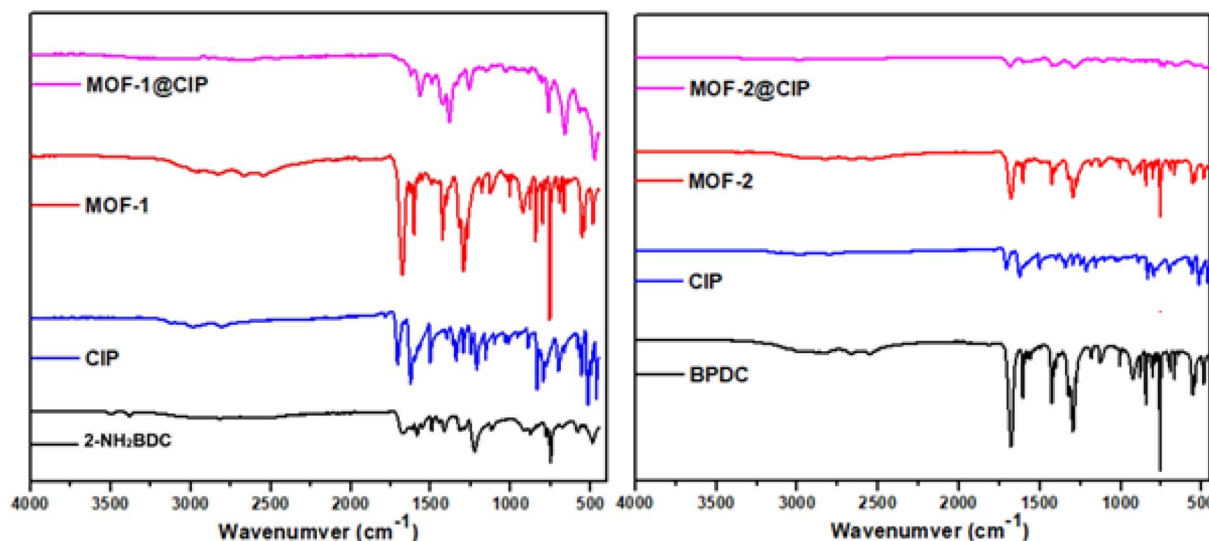Fig. 1 PXRD pattern of Zr-MOFs showing sharp and well-defined peaks.

Fig. 2 (a) FTIR spectra of 2-amino-BDC (2-amino-1,4-benzenedicarboxylic acid) ciprofloxacin (CIP), Zr-MOF-1, and Zr-MOF-1@CIP (ciprofloxacin encapsulated Zr-MOF-1) (b) FTIR spectra of BPDC (4,4′-biphenyldicarboxylic acid), Zr-MOF-2, ciprofloxacin (CIP) and Zr-MOF-2@CIP (ciprofloxacin encapsulated Zr-MOF-2).

both MOF-1 and MOF-2, with characteristic bands at 1622 cm^{-1} and 1384 cm^{-1} that match the CIP spectrum. The peak at 2822 cm^{-1} correspond to nitrogen–carbon bond stretching, while the C=O carbonyl stretch appears at 1687 cm^{-1}, and the carbon–nitrogen stretch is detected at 1472 cm^{-1}. A weak band observed at 1495 cm^{-1} suggests the presence of CIP drug. Furthermore, the IR spectra display the O–H bending of linker at 756 cm^{-1} and Zr–O stretching of metal-ions cluster at 668 cm^{-1}.

The IR spectra of MOF-1 and MOF-2 show high similarity due to the common functional groups present in both materials. Bands at 2944 cm^{-1} and 2866 cm^{-1} are associated with the asymmetrical and symmetrical CH$_2$ stretches, while the band at 1710 cm^{-1} indicates C=O carbonyl stretching in ciprofloxacin. The peak at 1297 cm^{-1} belongs to C–O and C–C stretching.

SEM analysis is crucial for drug delivery applications of Zr-MOFs, revealing key morphological and structural features that impact MOF-drug interactions (Fig. 3). SEM analysis of Zr-MOF-1 at magnifications of 1 μm and 2 μm shows block-like crystals with rectangular and cubic shapes. These crystals display multiple sizes, with an average dimension of around 0.176 μm, as determined through image analysis. While Zr-MOF-2 has elongated globular crystals with average size of about 0.696 μm.

The BET analysis of Zr-MOFs confirmed their meso-porosity as indicated by Type IV isotherms (Fig. 4a and c). Zr MOF-1 exhibited a lower BET area of 64.75 m^2 g^{-1} with an average pore-width 26.66 nm while Zr-MOF-2 demonstrated a higher surface area of 85.43 m^2 g^{-1} and a somewhat larger average pore
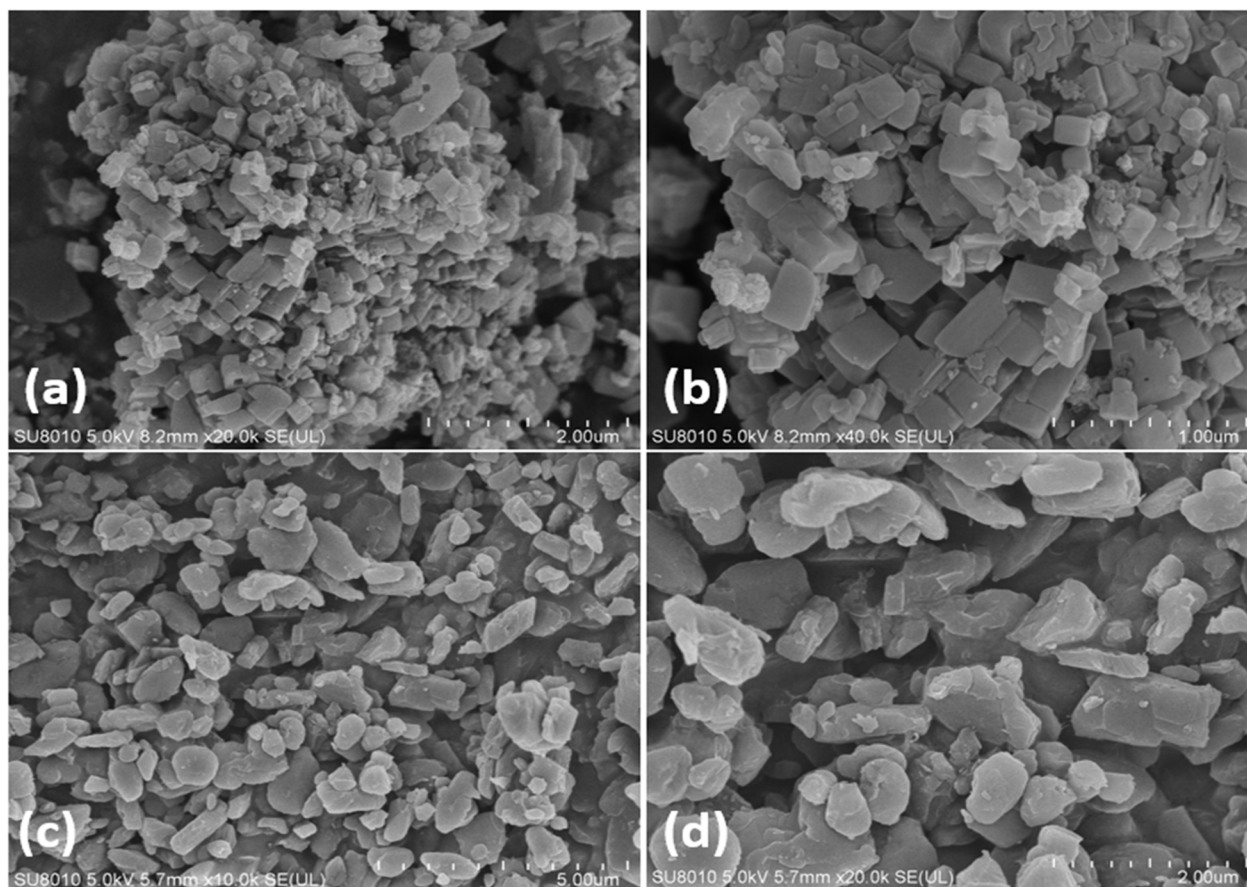
Fig. 3 The SEM micrograph image of the Zr-MOF-1 (a, b) and Zr-MOF-2 (c, d) at 2 μm and 1 μm.

width of 27.97 nm. Both Zr-MOFs displayed a predominantly 2–4 nm pore size distribution as indicated in by graph in Fig. 4b and d which confirm the presence of mesopores with the Zr-MOF framework structure. Ciprofloxacin is a relatively large molecule, measuring approximately 12 Å in length and 8 Å in width.

3.2 Loading of ciprofloxacin on Zr-MOFs

The efficient loading of drugs into metal–organic frameworks (Zr-MOFs) is critically influenced by the MOF's structural characteristics, such as surface area, pore size, and porosity, which determine the interaction dynamics between the drug molecules and the Zr-MOF framework. As depicted in Fig. 5, with MOF and drug ratio the loading efficiency increases progressively, reflecting a direct association between the ciprofloxacin content and its absorption by Zr-MOF because of maximum polar donor sites and appropriate pore-size in Zr-MOF channels (metal node and organic framework), ciprofloxacin is preferentially captured by the nanosized Zr-MOFs.

Zr-MOF-1, with a BET surface area of 64.75 m^2 g^{-1} and an average pore width of 26.66 nm, exhibits lower loading efficiencies of 66.33% at a 1:1 ratio, 69.57% at a 1:2 ratio, and 70.01% at a 1:3 ratio. The relatively smaller surface area of Zr-MOF-1 limits the number of available adsorption sites for

ciprofloxacin, which directly impacts its capacity to encapsulate higher drug concentrations. As a result, an increase in the drug ratio from 1:1 to 1:2 leads to only a moderate rise in loading efficiency, and the difference between 1:2 and 1:3 ratios become negligible. This saturation effect indicates that Zr-MOF-1 pores are quickly occupied at lower drug concentrations, and its limited surface area does not support a significant increase in loading as the drug concentration increases further. The relatively smaller average pore width of Zr-MOF-1 also contributes to this limitation, as it creates steric hindrance that prevents the effective encapsulation of additional ciprofloxacin molecules beyond a certain concentration.

The higher BET surface-area of Zr-MOF-2 (85.43 m^2 g^{-1}) compared to Zr-MOF-1 (64.75 m^2 g^{-1}) provides a more extensive network of adsorption sites for ciprofloxacin molecules, which leads to higher loading efficiencies. This is reflected in the observed loading efficiencies of Zr-MOF-2: 76.39% for a 1:1 MOF:drug ratio, 81.10% for a 1:2 ratio, and a remarkable 87.62% for a 1:3 ratio. Fig. 5 illustrates that the efficiency of drug loading rises by increasing drug ratio, demonstrating a straight relationship between ciprofloxacin quantity and its absorption by the Zr-MOF-2. This trend suggests that Zr-MOF-2 framework can accommodate additional drug molecules as the drug concentration increases, unlike Zr-MOF-1, which reaches a near-saturation point.
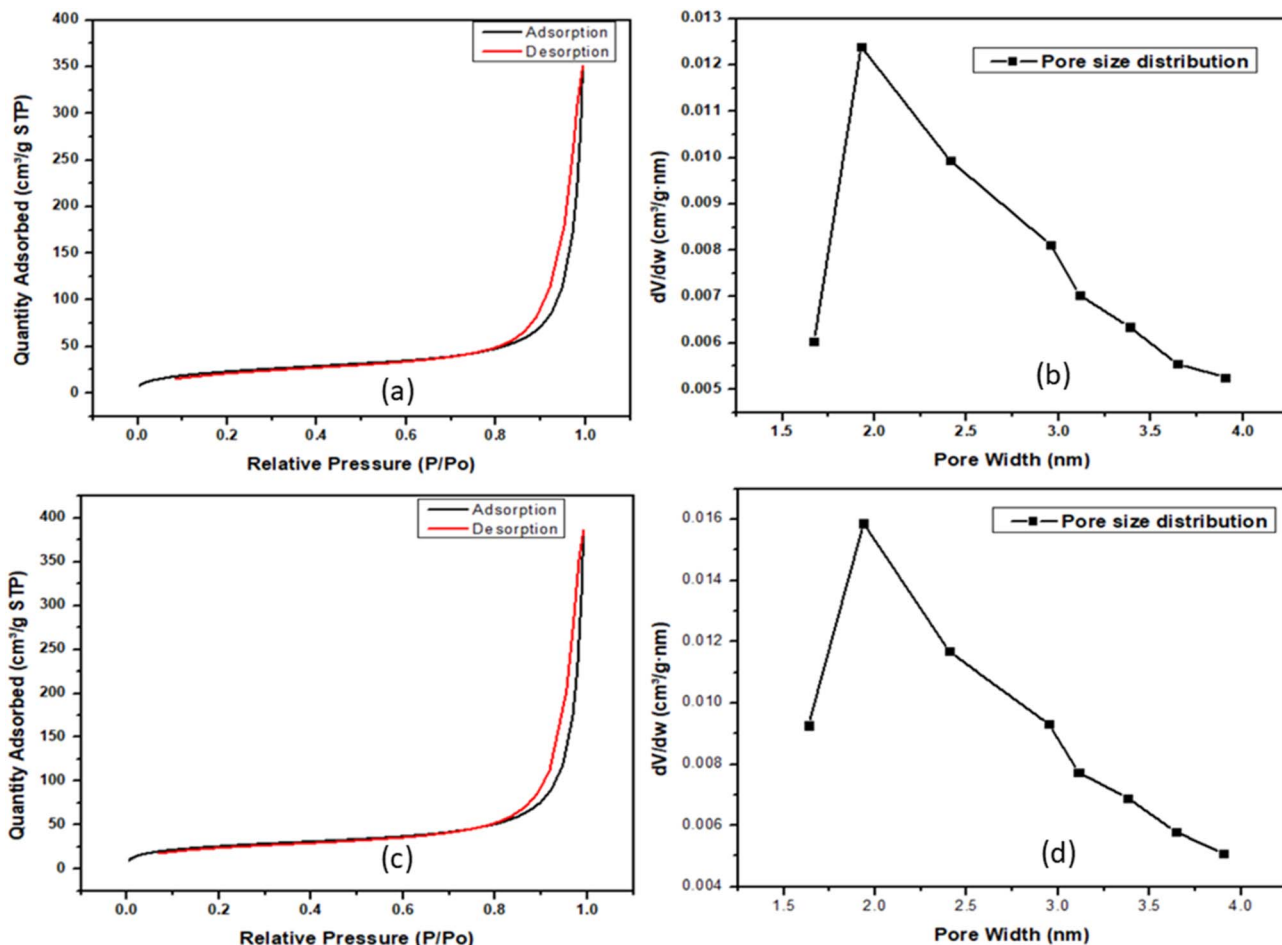
Fig. 4   BET nitrogen sorption isotherm of. Zr–MOF–1 (a) and Zr–MOF–2 (c); pore size distribution of Zr–MOF–1 (b) and Zr–MOF–2 (d).
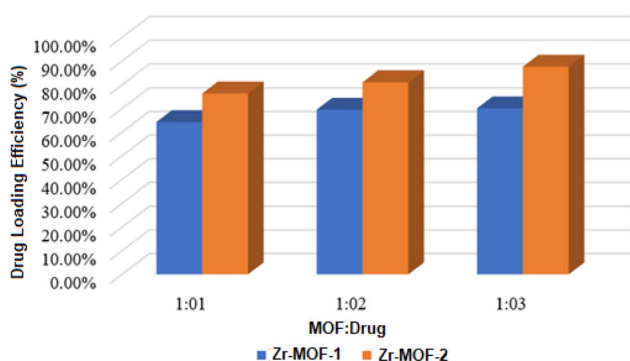

Fig. 5   Loading percentage of ciprofloxacin on Zr–MOF–1 and Zr–MOF–2 at different ratios.

The average pore width also plays a crucial role in drug encapsulation. Ciprofloxacin, with molecular dimensions of approximately 12 Å in length and 8 Å in width, requires sufficient pore space to be effectively encapsulated without significant steric hindrance. Zr-MOF-2 with an average pore width of 27.97 nm slightly bigger than Zr-MOF-1 26.66 nm is better to accommodate ciprofloxacin dimensions since it offers a wider pore size. The higher pore width of Zr-MOF-2 enhances the feasibility of ciprofloxacin molecules to enter and bind within Zr-MOF, which provides a way to minimize steric hindrance so that the encapsulation of the ciprofloxacin molecules is effective. As a result, Zr-MOF-2 with a higher pore size and surface area for drug loading shows better distribution of the drug molecules into their frameworks with improved efficiency of drug loading with the increasing concentration of drug.

Higher surface area and pore width of the Zr-MOF-2 as compared to Zr-MOF-1 is mainly due to its organic linkers. As compared to the smaller 2-amino BBC linker in Zr-MOF-1, BPDC is slightly larger and more rigid linker and increases the porosity of Zr-MOF-2 framework. The extended aromatic structure of BPDC forms larger channels and increased mesoporosity relative to the precursor or simply increased porosity. On the other hand, Zr-MOF-1 with a small 2-amino BDC linker compiles a denser mesh with small pore size which hinder the ability to encapsulate a high concentration of the drug.

In addition to higher surface area and optimal pore size, the uptake of ciprofloxacin drug is attributed to hydrogen bonding interaction between the Zr-MOFs functional groups and ciprofloxacin drug. In Zr-MOF-1, the amino groups from the 2-amino BDC linker indicate the potential of forming H-bonding

interaction with ciprofloxacin.[86–88] Although, such interactions can raise the first layer adsorption, the ability to load a drug molecule is restrained by the subsequent layers' lower surface area and pore volume. In Zr-MOF-2, its linker BPDC has a larger area of contact to engage in the π–π stacking and also carboxylic functional groups for hydrogen bonding. Maximum encapsulation/incorporation/adsorption of ciprofloxacin occur in Zr-MOF-2 for the reason that BET surface area, average pore width and linker size of Zr-MOF-2 is higher than Zr-MOF-1. These interactions facilitate better adsorption and encapsulation of ciprofloxacin, especially at higher drug concentrations, contributing to the progressive increase in loading efficiency observed with increasing MOF : drug ratio.

3.3 Release of encapsulated drug from Zr-MOFs

3.3.1 Effect of pH on drug release. Three different pH was chosen in our study as we know different parts of human digestive system (oral cavity, stomach, duodenum, small intestine, and colon) have different pH. Actually, oral drug passes through digestive tract, therefore our main focus was to find out the release efficiency of ciprofloxacin loaded MOFs at different pH. As appropriately noted, the controlled release rates of ciprofloxacin from the MOFs are reduced at neutral pH 7.4 and acidic pH 3.0, whereas the maximum release was witnessed at alkaline pH 9.2. We would like to clear up that the usage of pH 9.2 was not proposed to mimic normal physiological conditions, but somewhat to examine the pH-responsive release performance of the drug–MOF system in a range of pH

surroundings, together with those related to specific pathological or localized environments. Even though the systemic physiological pH is about 7.4, numerous studies have revealed that local microenvironments in disease states (*e.g.*, infected wounds, inflammatory tissues, and certain regions of the gastrointestinal tract such as the duodenum) may exhibit mildly alkaline conditions, where pH values can exceed 8.0. For example, chronic wound spots and bacterial infections (especially involving urease-producing bacteria like Proteus or Klebsiella) can raise local pH to ~8.5–9.0, which can assist the release of basic or zwitter ionic drugs like ciprofloxacin. The intestinal fluid in the duodenum and upper jejunum can range pH levels up to 8.0–8.5 in certain dietary or post-prandial environments. In this perspective, our synthesized Zr-MOFs shows promise for site-specific delivery, where the MOF arrangement remains stable but triggers burst drug release under mildly alkaline stimuli, making it appropriate for uses such as targeted intestinal delivery of ciprofloxacin, avoiding premature release in acidic gastric fluid (pH 1–3) and pH-sensitive wound dressings or coverings for infection-responsive drug delivery.

Fig. 6 refers to ciprofloxacin (CIP) release from drug loaded Zr-MOFs at three pH levels: 9.2, 7.4, and 3.0 over time. The maximum release was found at pH 9.2 while minimum release was observed at pH 3.0. This trend is because ciprofloxacin hydrochloride is acidic and more soluble in basic medium. At pH 9.2, ciprofloxacin deprotonates and hence its interaction with the MOF matrix decreases and it gets released more easily.
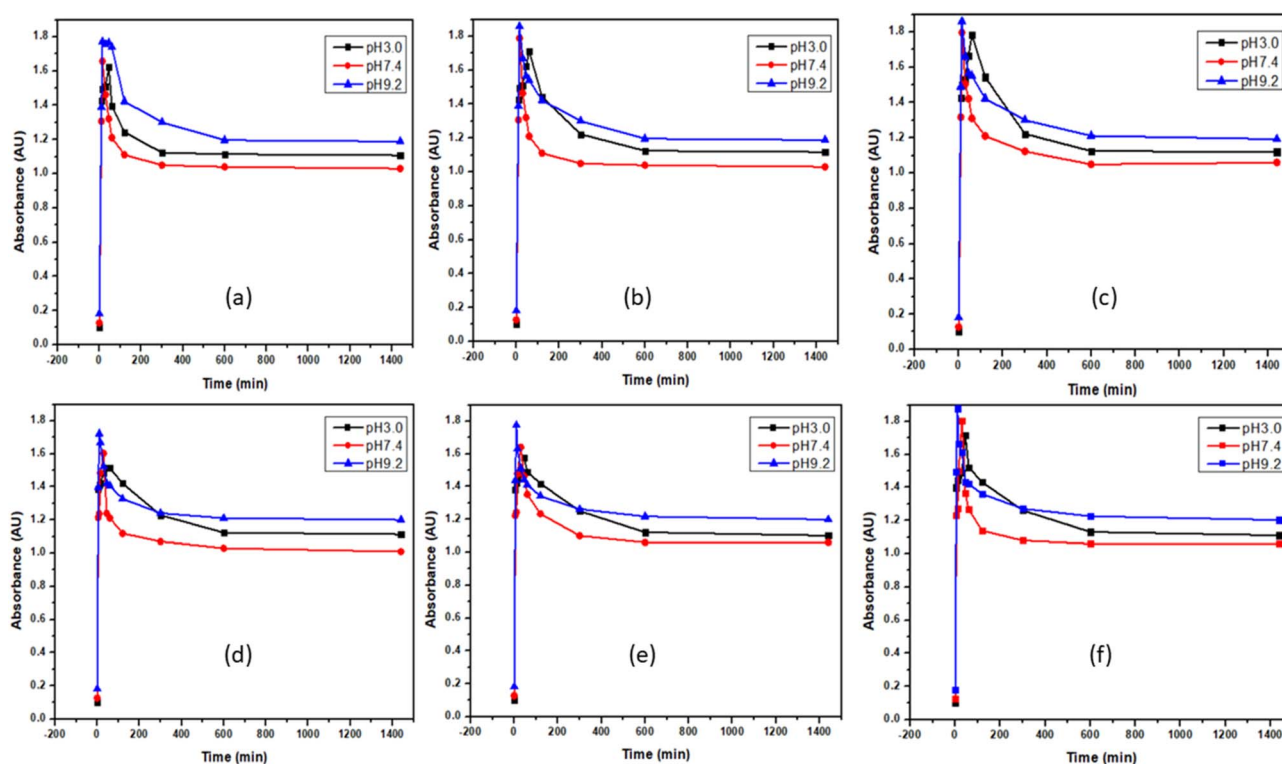

Fig. 6 Release profile of the ciprofloxacin from the Zr-MOF-1@CIP at different pHs with MOF : drug ratio 1 : 1 (a), 1 : 2 (b), 1 : 3 (c) and from Zr-MOF-2@CIP with MOF : drug ratio 1 : 1 (d) 1 : 2 (e) 1 : 3 (f).

The release rates of ciprofloxacin are reduced when the pH of the solution is lowered such as 7.4 and 3.0. It was also noted that at all the tested pH levels both Zr-MOFs exhibited an initial burst release, the effect that can be explained by physical adsorption, for instance, through the dipole–dipole and hydrogen bonding between ciprofloxacin and the MOF. Following the initial burst, the release profiles stabilize, with absorbance levels remaining relatively constant. This suggests that the majority of the drug is released within the first 60 minutes, and the remaining drug is tightly bound to the Zr-MOF. At pH 9.2, the burst release is more pronounced as the drug molecules deprotonate and rapidly desorb from the Zr-MOF surface.

3.3.2 Effect of drug concentration on drug release. The effect of concentration on release of drug from Zr-MOF@CIP is also observed by taking the absorbance of released solutions gradually. Each drug loading ratio displayed a rapid initial drug release, characterized by a rapid increase in absorbance at the beginning. It is attributed to ciprofloxacin that is present on the surface of the Zr-MOFs through weak interactions. Relatively higher burst release in case of 1 : 3 ratio as compared to the 1 : 1 and 1 : 2 ratios (Fig. 7) suggests that a greater drug loading results in a higher amount of ciprofloxacin being available for immediate release. This increased burst in the higher ratio is due to a larger quantity of drug molecules being located on or near the surface of the MOFs, where weak interactions allow for a faster release. The release profiles for all loading ratios gradually stabilized over time.

The impact of different MOF : drug ratios (1 : 1, 1 : 2, and 1 : 3) on ciprofloxacin release reveals important differences between Zr-MOF-1@CIP and Zr-MOF-2@CIP. For Zr-MOF-1@CIP, an initial burst of ciprofloxacin release was observed at all 1 : 1, 1 : 2 and 1 : 3 MOF : drug ratios, largely due to the rapid desorption of drug molecules from the Zr-MOF surface. However, for 1 : 2 and 1 : 3 MOF : drug ratios, the release profiles were more similar at all pHs. This trend indicates that Zr-MOF-1 relatively small surface area and pore volume were saturated, which limited the increase in drug release efficiency even at higher drug concentrations. Thus, the release rate did not significantly change with the higher drug concentration, leading to a more stable but less responsive release pattern. Zr-MOF-2@CIP showed a great increase in drug release with rising drug concentrations at all pHs. At the 1 : 3 ratio, Zr-MOF-2@CIP showed the highest release levels because the maximum quantity of drug was loaded on the Zr-MOFs at this ratio, driven by its larger surface area and pore volume. The initial burst release was also more pronounced in Zr-MOF-2@CIP across all ratios, particularly at 1 : 3, where the higher concentration of drug molecules led to a swift release followed by a steady, controlled release. This demonstrates the superior ability of Zr-MOF-2 to accommodate and release larger amounts of ciprofloxacin compared to Zr-MOF-1, reflecting its more efficient and adaptable structure. Zr-MOF-2, characterized by high porosity and non-toxic properties, has been utilized for ciprofloxacin storage and delivery. It also exhibits a moderately higher 5-Fu loading capability and a pH-responsive drug releasing profile.
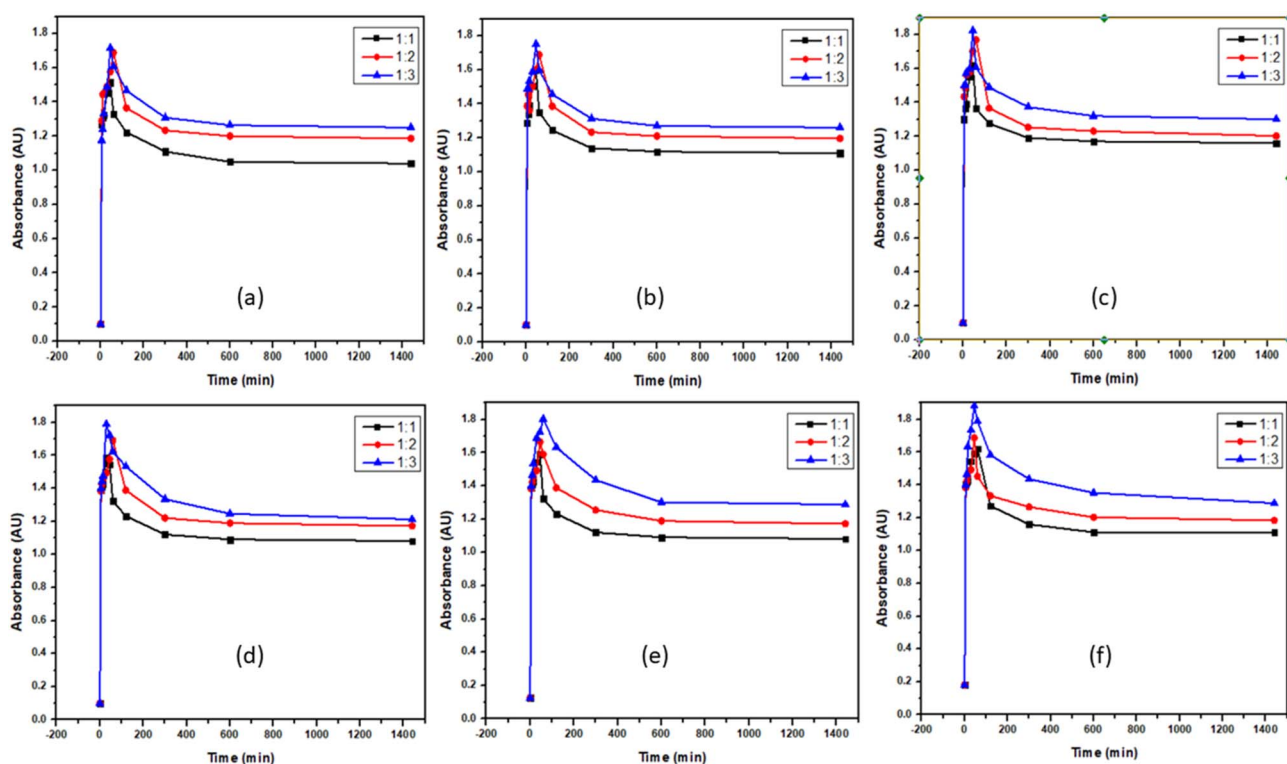

Fig. 7 Outcome of drug concentration on. Release of ciprofloxacin from Zr-MOF-1@CIP at (a) 3.0 (b) 7.4 (c) 9.2 and from Zr-MOF-2@CIP at pH (d) 3.0 (e) 7.4 (f) 9.2.
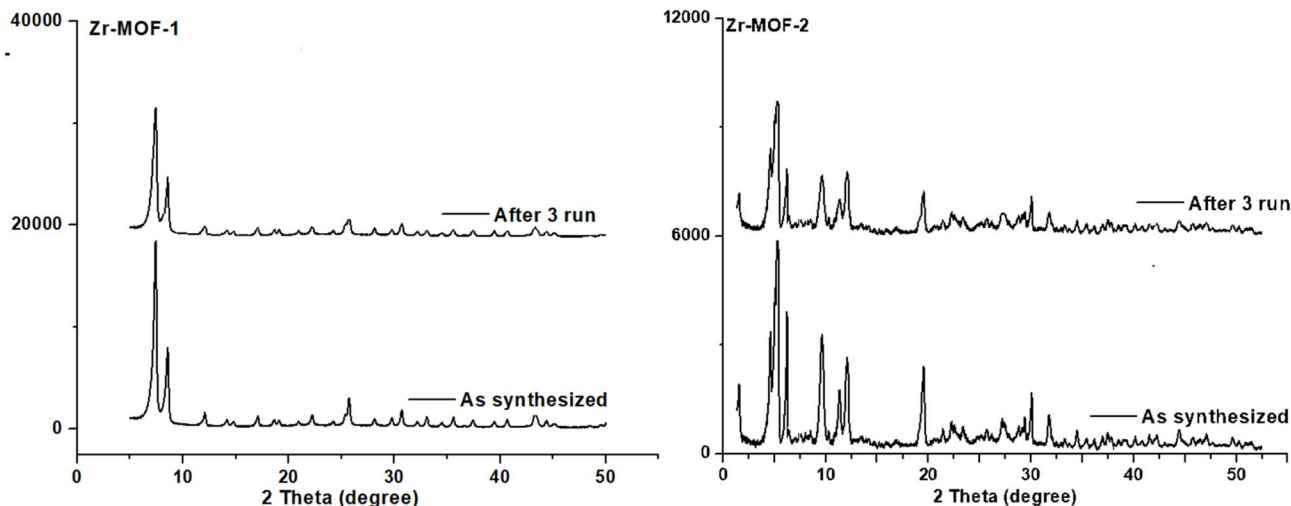
Fig. 8 PXRD patterns of Zr–MOFs pre and post drug encapsulation and successive release cycles.

The PXRD patterns from both the second and fresh runs displayed consistent results, indicating that the Zr-MOFs maintained their chemical stability. The PXRD analysis of Zr-MOFs confirmed that their core structure remained intact after the second recycling (Fig. 8). This demonstrated that the Zr-MOFs could be effectively reused for up to three cycles. Further PXRD analysis of the recycled Zr-MOFs showed that their structural integrity was preserved throughout the drug encapsulation and release processes.

3.4 Comparative study of drug release

The higher amount of ciprofloxacin was released at pH 9.2 as related to the pH 7.4 and pH 3.0. This increased release is ascribed to higher solubility of the ciprofloxacin hydrochloride at elevated pH, which reduces its interaction with the MOF. Additionally, the partial hydrolysis of Zr-MOF@CIP in basic environments may contribute to the enhanced release. Conversely, the lowest release was observed at pH 3.0 because of low solubility of ciprofloxacin hydrochloride in acidic medium. At pH 7.4, the release was moderate, corresponding to physiological conditions. The amount of ciprofloxacin released was proportional to the initial loading, with the 1 : 2 ratio exhibiting a higher burst release than 1 : 1 but lower than 1 : 3. This pH-responsive behavior, coupled with the nano-carrier's low toxicity, underscores its potential for effective antibiotic delivery in future applications.

Zr-MOF-1, synthesized *via* 2-amino-1,4-benzenedicarboxylic acid (NH$_2$-BDC), and Zr-MOF-2, based on 4,4′-biphenyldicarboxylic acid (BPDC), vary meaningfully in terms of their structural dimensionality, pore volume, and surface characteristics. Zr-MOF-1 incorporates a relatively shorter linker (NH$_2$-BDC), causing in reduced pore windows, smaller linker size, and inferior surface area, which fundamentally restricts the lodgings of bigger drug molecules like ciprofloxacin. Zr-MOF-2, on the other hand, consists of BPDC, a lengthier, more hydrophobic linker, which adds to larger pore apertures and enhanced porosity, thereby permitting superior drug diffusion

and entrapment. These structural features directly impact the drug loading proficiency, with Zr-MOF-2 representing considerably greater loading related to Zr-MOF-1, likely due to improved π–π stacking among the aromatic quinolone ring of the ciprofloxacin and the prolonged biphenyl linkers in BPDC, amplified surface interactions due to greater surface area, larger organic linker size, pore volume and reduced steric hindrance during encapsulation. Additionally, ciprofloxacin a fluoroquinolone antibiotic satisfies Lipinski's Rule of Five (Pfizer rule), due to its molecular weight 331.3 g mol^{-1} (<500 g mol^{-1}), hydrogen bond donors: 2 (acceptable <5), hydrogen bond acceptors: 6 (acceptable <10), log$P$: ~0.28 (acceptable <5). Therefore, ciprofloxacin is moderately hydrophilic, presenting it suitable for interaction with Zr-MOFs comprising both hydrophilic as well as hydrophobic domains. Larger and more hydrophobic framework of Zr-MOF-2 accommodates this duality in a better way, improving encapsulation and controlled release. The release performance was studied at three physiologically relevant pH conditions 3.0, 7.4, and 9.2. At pH 3.0 (acidic), both MOFs exhibited negligible release due to protonation of ciprofloxacin's carboxyl group, leading to reduced solubility and stronger electrostatic interaction with the Zr-node. At pH 7.4 (physiological), moderate release was observed due to partial ionization of ciprofloxacin and the MOF linkers.

At pH 9.2 (alkaline), Zr-MOF-2 demonstrated the uppermost release, which can be endorsed to deprotonation of ciprofloxacin, improving its solubility, weakened host–guest interactions, supporting drug diffusion and stability of Zr-MOF-2 in basic medium, permitting sustained release deprived of framework degradation. A previous study showed that stability of Zr-MOF is sustained by no significant leaching or soluble Zr^{4+} detected in the solution over the pH range of 1 to 12. On the other hand, the instability of Zr MOFs above pH 12 was accompanied by the absence of soluble Zr^{4+} by ICP-OES analysis of supernatants which can be attributed to the formation of zirconium oxide/hydroxide solids at pH greater than 12.[89,90] Zr-

MOF-1 showed inferior release efficiency at the same pH, conceivably due to tighter packing inside smaller pores, hydrogen bonding involving the $-NH_2$ group of BDC linkers which may hold ciprofloxacin more strappingly.

To study deeper insight into the release behavior of ciprofloxacin from Zr-MOF-1 and Zr-MOF-2, the *in vitro* drug release profiles were built-in to numerous kinetic models, including zero-order, first-order, Higuchi, and Korsmeyer–Peppas models. For both MOFs, the Korsmeyer–Peppas model provided the best fit ($R^2 > 0.98$), indicating a non-Fickian transport mechanism. This put forward that drug discharge from these systems is governed by a combination of diffusion through the porous framework and gradual erosion or swelling of the MOF matrix in aqueous media. Conspicuously, Zr-MOF-2 demonstrated a greater release exponent ($n \sim 0.62$) compared to Zr-MOF-1 ($n \sim 0.45$), suggesting a greater involvement of matrix relaxation procedures in the release dynamics of the former, which can be endorsed to its superior structural flexibility and larger pore volume.

When compared with other zirconium-based MOFs reported in the literature such as copper-glutamate-MOF,[91] UiO-66,[92] ZIF-8,[93] Fe_3O_4@PAA@ZIF8,[94] Co-MOF/PLA,[95] and MIL-101(Fe);[96] the performance of Zr-MOF-2 is predominantly noteworthy. While UiO-66-type MOFs normally based on BDC offer extraordinary thermal and aqueous stability, their restricted pore size often limits proficient encapsulation and sustained release of larger drugs. In contrast, Zr-MOF-2, based on the extended BPDC linker, provides a categorized porous structure that accelerates both higher loading capacity and enhanced release efficiency at pH 9.2. Furthermore, compared to MIL-101(Fe), which often shows burst release due to mesoporosity and poor framework stability under alkaline conditions, Zr-MOF-2 retains structural integrity and delivers the drug in a more controlled manner.

4 Conclusion

In this study, we successfully synthesized two Zr based MOFs and evaluated their capabilities for targeted ciprofloxacin delivery. The results showed that Zr-MOF-2 exhibited superior drug-loading efficiency and enhanced release control compared to Zr-MOF-1. The release of ciprofloxacin from Zr-MOF-2@CIP followed a more predictable, ensuring a quantifiable and controlled drug delivery process. Conversely, Zr-MOF-1 was less effective in both drug loading and drug release performance. Therefore, this study highlights Zr-MOF-2 as an optimized platform for sustained and selective ciprofloxacin delivery, offering a significant advancement in controlled drug release systems. Future studies will focus on further enhancing the textural properties of Zr-MOF-2 to maximize drug encapsulation efficiency. Additionally, cytotoxicity assessments in cell culture models will be conducted to evaluate its biocompatibility. There by advancing its potential for clinical applications.

Data availability

The data used to support the finding of this study was included within the manuscript.

Conflicts of interest

There are no conflicts of interest to declare.

Notes and references

1 G. B. Mahady, *Curr. Pharm. Des.*, 2005, **11**, 2405–2427.
2 M. Lobanovska and G. Pilla, *Yale J. Biol. Med.*, 2017, **90**, 135.
3 A. D. Pranger, J. W. C. Alffenaar and R. E. Aarnoutse, *Curr. Pharm. Des.*, 2011, **17**, 2900–2930.
4 D. C. Hooper and G. A. Jacoby, *Cold Spring Harbor Perspect. Med.*, 2016, **6**, a025320.
5 V. Chandrakala, V. Aruna and G. Angajala, *Emergent Mater.*, 2022, **5**, 1593–1615.
6 M. H. Karami, M. Abdouss and B. Maleki, *Nanomed. J.*, 2024, **11**, 222.
7 B. A. Aderibigbe, *Molecules*, 2017, **22**, 1370.
8 R. C. Huxford, J. Della Rocca and W. Lin, *Curr. Opin. Chem. Biol.*, 2010, **14**, 262–268.
9 Z. Zhang, D. He, S. Zhao and J. Qu, *Toxics*, 2023, **11**, 692.
10 A. Mokhtarzadeh, A. Alibakhshi, M. Hejazi, Y. Omidi and J. E. N. Dolatabadi, *TrAC, Trends Anal. Chem.*, 2016, **82**, 367–384.
11 E. V. Batrakova, T. K. Bronich, J. A. Vetro and A. V. Kabanov, in *Nanoparticulates as drug carriers*, World Sci., 2006, pp. 57–93.
12 S. S. Davis and L. Illum, *Biomaterials*, 1988, **9**, 111–115.
13 U. Uthappa, O. Arvind, G. Sriram, D. Losic, M. Kigga and M. D. Kurkuri, *J. Drug Delivery Sci. Technol.*, 2020, **60**, 101993.
14 R. Kaur and I. Badea, *Int. J. Nanomed.*, 2013, **8**, 203–220.
15 X. Wu, Y. Li, F. Raza, X. Wang, S. Zhang, R. Rong, M. Qiu and J. Su, *Pharmaceutics*, 2021, **13**, 99.
16 J. Duan, Y. Sun, S. Chen, X. Chen and C. Zhao, *J. Mater. Chem. A*, 2020, **8**, 18810–18815.
17 H. Zhang, Q. Zhang, C. Liu and B. Han, *Biomater. Sci.*, 2019, **7**, 1696–1704.
18 M. J. Molaei, *J. Drug Delivery Sci. Technol.*, 2021, **61**, 101830.
19 X. Mei, T. Hu, Y. Wang, X. Weng, R. Liang and M. Wei, *Wiley Interdiscip. Rev.: Nanomed.*, 2020, **12**, e1596.
20 C. Sarkar, A. R. Chowdhuri, S. Garai, J. Chakraborty and S. K. Sahu, *Cellulose*, 2019, **26**, 7253–7269.
21 J. R. Holst and A. I. Cooper, *Adv. Mater.*, 2010, **22**, 5212–5216.
22 D. J. Tranchemontagne, J. R. Hunt and O. M. Yaghi, *Tetrahedron*, 2008, **64**, 8553–8557.
23 H. Daglar, H. C. Gulbalkan, G. Avci, G. O. Aksu, O. F. Altundal, C. Altintas, I. Erucar and S. Keskin, *Angew. Chem., Int. Ed.*, 2021, **60**, 7828–7837.
24 W. Fan, X. Zhang, Z. Kang, X. Liu and D. Sun, *Coord. Chem. Rev.*, 2021, **443**, 213968.

25 H. Li, L. Li, R.-B. Lin, W. Zhou, Z. Zhang, S. Xiang and B. Chen, *EnergyChem*, 2019, **1**, 100006.

26 J.-R. Li, R. J. Kuppler and H.-C. Zhou, *Chem. Soc. Rev.*, 2009, **38**, 1477–1504.

27 S. Nandi, P. De Luna, T. D. Daff, J. Rother, M. Liu, W. Buchanan, A. I. Hawari, T. K. Woo and R. Vaidhyanathan, *Sci. Adv.*, 2015, **1**, e1500421.

28 X. Y. Dong, H. L. Huang, J. Y. Wang, H. Y. Li and S. Q. Zang, *Chem. Mater.*, 2018, **30**, 2160–2167.

29 D. Wu, P. F. Zhang, G. P. Yang, L. Hou, W. Y. Zhang, Y. F. Han, P. Liu and Y. Y. Wang, *Coord. Chem. Rev.*, 2021, **434**, 213709.

30 M. R. Saeb, N. Rabiee, M. Mozafari, F. Verpoort, L. G. Voskressensky and R. Luque, *Materials*, 2021, **14**, 7277.

31 X. Li, Z. Ma, H. Wang, Q. Shi, Z. Xie and J. Yu, *Coord. Chem. Rev.*, 2024, **514**, 215943.

32 H. Zhang, J. Nai, L. Yu and X. W. D. Lou, *Joule*, 2017, **1**, 77–107.

33 K. Jayaramulu, S. Mukherjee, D. M. Morales, D. P. Dubal, A. K. Nanjundan, A. Schneemann, J. Masa, S. Kment, W. Schuhmann and M. Otyepka, *Chem. Rev.*, 2022, **122**, 17241–17338.

34 O. Shekhah, J. Liu, R. Fischer and C. Wöll, *Chem. Soc. Rev.*, 2011, **40**, 1081–1106.

35 C. Petit, *Curr. Opin. Chem. Eng.*, 2018, **20**, 132–142.

36 A. E. Thorarinsdottir and T. D. Harris, *Chem. Rev.*, 2020, **120**, 8716–8789.

37 J. P. Zhao, Q. Yang, Z. Y. Liu, R. Zhao, B. W. Hu, M. Du, Z. Chang and X. H. Bu, *Chem. Commun.*, 2012, **48**, 6568–6570.

38 P. Lama, J. Mrozinski and P. K. Bharadwaj, *Cryst. Growth Des.*, 2012, **12**, 3158–3168.

39 S. Chaemchuen, N. A. Kabir, K. Zhou and F. Verpoort, *Chem. Soc. Rev.*, 2013, **42**, 9304–9332.

40 A. H. Chughtai, N. Ahmad, H. A. Younus, A. Laypkov and F. Verpoort, *Chem. Soc. Rev.*, 2015, **44**, 6804–6849.

41 Y.-S. Wei, M. Zhang, R. Zou and Q. Xu, *Chem. Rev.*, 2020, **120**, 12089–12174.

42 S. Afaq, M. U. Akram, W. M. A. Malik, M. Ismail, A. Ghafoor, M. Ibrahim, M. u. Nisa, M. N. Ashiq, F. Verpoort and A. H. Chughtai, *ACS Omega*, 2023, **8**, 6638–6649.

43 A. Paul, P. Liu, A. G. Mahmoud, L. Rakočević, E. C. Alegria, R. A. Khan, M. F. C. G. da Silva, Z. Wang and A. J. Pombeiro, *Chemosphere*, 2024, **364**, 143001.

44 M. D. Allendorf, C. A. Bauer, R. Bhakta and R. Houk, *Chem. Soc. Rev.*, 2009, **38**, 1330–1352.

45 H. Ōkawa, M. Sadakiyo, T. Yamada, M. Maesato, M. Ohba and H. Kitagawa, *J. Am. Chem. Soc.*, 2013, **135**, 2256–2262.

46 W. P. Lustig, S. Mukherjee, N. D. Rudd, A. V. Desai, J. Li and S. K. Ghosh, *Chem. Soc. Rev.*, 2017, **46**, 3242–3285.

47 P. Horcajada, C. Serre, M. Vallet-Regí, M. Sebban, F. Taulelle and G. Férey, *Angew. Chem., Int. Ed.*, 2006, **118**, 6120–6124.

48 M. U. Akram, M. Nesrullah, S. Afaq, W. M. A. Malik, A. Ghafoor, M. Ismail, H. Nawaz, M. Ibrahim, F. Verpoort and A. H. Chughtai, *New J. Chem.*, 2024, **48**, 11542–11554.

49 M. Ding, R. W. Flaig, H.-L. Jiang and O. M. Yaghi, *Chem. Soc. Rev.*, 2019, **48**, 2783–2828.

50 Y. Fang, Y. Ma, M. Zheng, P. Yang, A. M. Asiri and X. Wang, *Coord. Chem. Rev.*, 2018, **373**, 83–115.

51 M. M. Sirati, D. Hussain, K. Mahmood, A. H. Chughtai, M. Yousaf-Ur-Rehman, W. M. A. Malik, S. Alomairy, S. b. Ahmed, M. Al-Buriahi and M. N. Ashiq, *J. Taibah Univ. Sci.*, 2022, **16**, 525–534.

52 A. Paul, K. Radinović, S. Hazra, D. Mladenović, B. Šljukić, R. A. Khan, M. F. C. Guedes da Silva and A. J. Pombeiro, *Molecules*, 2022, **27**, 7323.

53 M. Nadeem, G. Yasin, M. H. Bhatti, M. Mehmood, M. Arif and L. Dai, *J. Power Sources*, 2018, **402**, 34–42.

54 W. M. Ahmed Malik, S. Afaq, A. Mahmood, L. Niu, M. Yousaf ur Rehman, M. Ibrahim, A. Mohyuddin, A. M. Qureshi, M. N. Ashiq and A. H. Chughtai, *Front. Chem.*, 2022, **10**, 996560.

55 M. Yousaf ur Rehman, D. Hussain, S. Abbas, A. M. Qureshi, A. H. Chughtai, M. Najam-Ul-Haq, A. S. Alsubaie, S. Manzoor, K. H. Mahmoud and M. N. Ashiq, *J. Taibah Univ. Sci.*, 2021, **15**, 637–648.

56 N. Nazar, S. Manzoor, Y. ur Rehman, I. Bibi, D. Tyagi, A. H. Chughtai, R. S. Gohar, M. Najam-Ul-Haq, M. Imran and M. N. Ashiq, *Fuel*, 2022, **307**, 121823.

57 M. Y. ur Rehman, S. Manzoor, N. Nazar, A. G. Abid, A. M. Qureshi, A. H. Chughtai, K. S. Joya, A. Shah and M. N. Ashiq, *J. Alloys Compd.*, 2021, **856**, 158038.

58 A. Paul, F. Gusmão, A. G. Mahmoud, S. Hazra, L. Rakočević, B. Šljukić, R. A. Khan, M. F. C. G. da Silva and A. J. Pombeiro, *CrystEngComm*, 2024, **26**, 2755–2764.

59 H. Konnerth, B. M. Matsagar, S. S. Chen, M. H. Prechtl, F.-K. Shieh and K. C.-W. Wu, *Coord. Chem. Rev.*, 2020, **416**, 213319.

60 A. Thakur and A. Kumar, *Sci. Total Environ.*, 2022, **834**, 155219.

61 A. Vaseashta, M. Vaclavikova, S. Vaseashta, G. Gallios, P. Roy and O. Pummakarnchana, *Sci. Technol. Adv. Mater.*, 2007, **8**, 47.

62 B. Jiang, L. Lian, Y. Xing, N. Zhang, Y. Chen, P. Lu and D. Zhang, *Environ. Sci. Pollut. Res.*, 2018, **25**, 30863–30879.

63 F. D. Duman and R. S. Forgan, *J. Mater. Chem.*, 2021, **9**, 3423–3449.

64 D. K. Yoo, H. C. Woo and S. H. Jhung, *Coord. Chem. Rev.*, 2020, **422**, 213477.

65 X. Zhu, Z. Fan, X.-F. Zhang and J. Yao, *J. Colloid Interface Sci.*, 2023, **629**, 182–188.

66 K. Zhang, Q. Huo, Y. Y. Zhou, H. H. Wang, G. P. Li, Y. W. Wang and Y. Y. Wang, *ACS Appl. Mater. Interfaces*, 2019, **11**, 17368–17374.

67 J. Y. An, S. J. Geib and N. L. Rosi, *J. Am. Chem. Soc.*, 2009, **131**, 8376.

68 O. M. Yaghi, G. Li and H. Li, *Nature*, 1995, **378**, 703–706.

69 M. R. Mehmandoust, N. Motakef-Kazemi and F. Ashouri, *Iran. J. Sci. Technol., Trans. A: Sci.*, 2019, **43**, 443–449.

70 C. Y. Sun, C. Qin, C. G. Wang, Z. M. Su, S. Wang, X. L. Wang, G. S. Yang, K. Z. Shao, Y. Q. Lan and E. B. Wang, *Adv. Mater.*, 2011, **23**, 562932.

71 Q. Hu, J. Yu, M. Liu, A. Liu, Z. Dou and Y. Yang, *J. Med. Chem.*, 2014, **57**, 5679–5685.

72 K. Jiang, W. Ni, X. Cao, L. Zhang and S. Lin, *Mater. Today Bio*, 2022, **13**, 100180.

73 H. Dong, G. X. Yang, X. Zhang, X. B. Meng, J. L. Sheng, X. J. Sun, Y. J. Feng and F. M. Zhang, *Chem.–Eur. J.*, 2018, **24**, 17148–17154.

74 J. H. Cavka, S. Jakobsen, U. Olsbye, N. Guillou, C. Lamberti, S. Bordiga and K. P. Lillerud, *J. Am. Chem. Soc.*, 2008, **130**, 13850–13851.

75 C. E. Ferreira, S. S. Balula and L. Cunha-Silva, *Compounds*, 2024, **4**, 315–337.

76 Y. Bai, Y. Dou, L. H. Xie, W. Rutledge, J. R. Li and H. C. Zhou, *Chem. Soc. Rev.*, 2016, **45**, 2327–2367.

77 D. Zou and D. Liu, *Mater. Today Chem.*, 2019, **12**, 139–165.

78 T. L. Tan, M. A. bin Mohammad Latif and S. A. Rashid, *J. Solid State Chem.*, 2022, **315**, 123429.

79 X. Su, T. Xu, R. Ye, C. Guo, S. M. Wabaidur, D. L. Chen, S. Aftab, Y. Zhong and Y. Hu, *J. Colloid Interface Sci.*, 2023, **646**, 129–140.

80 M. D. Goudarzi, M. B. Sabouti, N. Khosroshahi and V. Safarifard, *New J. Chem.*, 2023, **47**, 7335–7345.

81 J. S. Choi, J. Bae, E. J. Lee and N. C. Jeong, *Inorg. Chem.*, 2018, **57**, 5225–5231.

82 Y. Yang, P. Shukla, S. Wang, V. Rudolph, X.-M. Chen and Z. Zhu, *RSC Adv.*, 2013, **3**, 17065–17072.

83 M. J. Katz, Z. J. Brown, Y. J. Colón, P. W. Siu, K. A. Scheidt, R. Q. Snurr, J. T. Hupp and O. K. Farha, *Chem. Commun.*, 2013, **49**, 9449–9451.

84 R. Verma, G. Dhingra, G. Singh, J. Singh, N. Dureja and A. K. Malik, *J. Fluoresc.*, 2024, **34**, 1631–1642.

85 X. Q. Zhan, F. C. Tsai, L. Xie, K. D. Zhang, H. L. Liu, N. Ma, D. Shi and T. Jiang, *Nanomaterials*, 2018, **8**, 655.

86 F. Parsa, M. Setoodehkhah and S. M. Atyabi, *Inorg. Chem. Commun.*, 2023, **155**, 111056.

87 Q. Yang, H. Yu, Y. He, Z. Liu, C. Qin, B. Liu and Y. Li, *Eur. Polym. J.*, 2020, **123**, 109445.

88 T. Li, L. X. Zhang, Y. Xing, H. Xu, Y. Q. Yue, Q. Li, H. Dong, H. Y. Wang and Y. Y. Yin, *Inorg. Chem. Commun.*, 2019, **108**, 107541.

89 T. Kobayashi, T. Sasaki, I. Takagi and H. Moriyama, *J. Nucl. Sci. Technol.*, 2007, **44**, 90–94.

90 S. Yuan, J. Peng, Y. Zhang and Y. Shao-Horn, *J. Phys. Chem. C*, 2019, **123**, 28266–28274.

91 M. D. Olawale, A. C. Tella, J. A. Obaleye and J. S. Olatunji, *New J. Chem.*, 2020, **44**, 3961–3969.

92 M. Nasrabadi, M. A. Ghasemzadeh and M. R. Z. Monfared, *New J. Chem.*, 2019, **43**, 16033–16040.

93 V. C. Ramos, C. B. G. Reyes, G. M. García, M. I. S. Quesada, F. J. M.-C. Barrero, J. J. S. Rábago and M. S. Polo, *Pharmaceutics*, 2022, **14**, 2546.

94 M. Esfahanian, M. A. Ghasemzadeh and S. M. H. Razavian, *Artif. Cells, Nanomed., Biotechnol.*, 2019, **47**, 2024–2030.

95 M. Yahyapour, M. Ranjbar and A. Mohadesi, *J. Mater. Sci.:Mater. Electron.*, 2021, **32**, 3180–3190.

96 M. Beiranvand, S. Farhadi and A. Mohammadi-Gholami, *RSC Adv.*, 2022, **12**, 34438–34453.